



PAPER

Atherosclerotic carotid bifurcation phantoms with stenotic soft inclusions for ultrasound flow and vessel wall elastography imaging

Boris Chayer¹, Marcel van den Hoven^{1,2}, Marie-Hélène Roy Cardinal¹, Hongliang Li^{1,3}, Abigail Swillens⁴, Richard Lopata²  and Guy Cloutier^{1,3,5,6} ¹ Laboratory of Biorheology and Medical Ultrasonics, University of Montreal Hospital Research Center (CRCHUM), Montreal, Quebec, Canada² Department of Biomedical Engineering, Eindhoven University of Technology, Eindhoven, The Netherlands³ Institute of Biomedical Engineering, University of Montreal, Montreal, Quebec, Canada⁴ IBiTech-bioMMeda, Ghent University, Ghent, Belgium⁵ Department of Radiology, Radio-oncology and Nuclear Medicine, University of Montreal, Montreal, Quebec, Canada⁶ Author to whom any correspondence should be addressed.E-mail: guy.cloutier@umontreal.ca**Keywords:** vascular phantom, carotid atherosclerotic plaque, duplex ultrasound, shear wave elastography, strain elastography, flow loop experiments, phantom fabrication processRECEIVED
30 October 2018REVISED
18 March 2019ACCEPTED FOR PUBLICATION
20 March 2019PUBLISHED
2 May 2019**Abstract**

As the complexity of ultrasound signal processing algorithms increases, it becomes more difficult to demonstrate their added value and thus robust validation strategies are required. We propose a method of manufacturing ultrasonic vascular phantoms mimicking an atheromatous plaque in an internal carotid artery bifurcation for applications in flow imaging and elastography. During the fabrication process, a soft inclusion mimicking a stenotic lipid pool was embedded within the vascular wall. Mechanical testing measured Young's moduli of the vascular wall and soft inclusion at 342 ± 25 kPa and 17 ± 3 kPa, respectively. B-mode, color Doppler, power Doppler, shear wave elastography, and strain elastography images of the different phantoms were produced to show the validity of the fabrication process. Because of their realistic geometries and mechanical properties, those phantoms may become advantageous for fluid-structure experimental modeling and validation of new ultrasound-based imaging technologies.

1. Introduction

Nowadays, new ultrasonic imaging modalities are developed for different applications. Non-invasive imaging methods such as vector flow mapping (Ekroll *et al* 2013, Pedersen *et al* 2014, Yiu *et al* 2014), pulse wave imaging (Shahmirzadi *et al* 2012), shear wave elastography (Couade *et al* 2010), natural pulsation elastography (Mercure *et al* 2014, Fekkes *et al* 2018, Nayak *et al* 2018), and vascular modulography (Porée *et al* 2017) have appeared in less than a decade for vascular applications or matured to get closer to clinical use (Nandlall and Konofagou 2016, Cloutier *et al* 2018). All these methods required phantom experiments as a first step validation. Moreover, they are often based on mechanical assumptions that are difficult to validate *in vivo*. Because new beamforming strategies allowing ultrafast imaging now provide the opportunity of developing duplex flow and elastography modes, there is a need for new phantom designs coupling flow and vessel wall dynamics.

Among carotid artery phantoms proposed in the literature for ultrasound applications, several rectilinear designs were conceptualized for flow and elastography imaging studies. A simplified geometry with a multilayer polyvinyl alcohol cryogel (PVA-C) design was used to construct arterial phantoms with non-homogeneous elasticity (Brusseu *et al* 2001). Our team created rectilinear vascular PVA-C phantoms containing soft and calcification-like inclusions to mimic diseased carotid arteries (Porée *et al* 2015, 2017). O'Flynn *et al* (2005) proposed a transparent carotid bifurcation phantom made of PVA-C to teach vascular catheterization. An agar-based bifurcation phantom containing a thin silicon vessel wall was developed for Doppler flow studies (Poepping *et al* 2004). The challenge of obtaining nonplanar lumen geometries corresponding to a real anthropomorphic stenosed carotid bifurcation artery was addressed using a low-melting point metal alloy core (Meagher *et al* 2007).

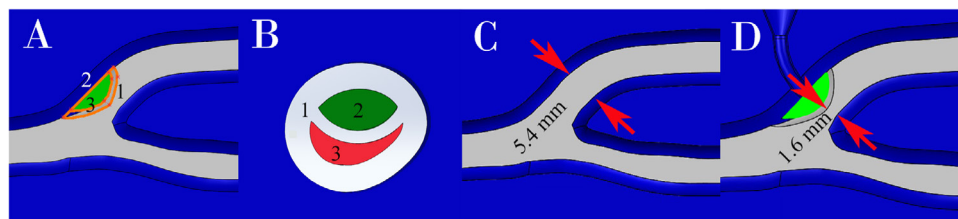


Figure 1. 3D rendering of the carotid bifurcation and plaque used for manufacturing the lumen stem (gray), the pouch for the soft inclusion (green), and external mold geometries (blue). On panel (A), one could see orange splines (labels 1 and 3) that were used to create the plaque and the soft inclusion by imposing a revolution around the axis (label 2). Panel (B) shows the cross-section of the mold at the 70% stenosis. The atheroma cap is surrounded by the wall (label 1) and corresponds to the part between the soft inclusion (label 2) and the lumen of the phantom (label 3). In panels (C) and (D), the arrow shows the position of the minimum lumen diameter at the bulb for the healthy and the 70% stenosis geometry, respectively.

Lai *et al* (2013) relied on a compliant three-dimensional (3D) prototyping material to fabricate complex carotid vessel geometries but this design resulted in strong attenuation on ultrasound images. More recently, a carotid bifurcation phantom was designed to study fluid-wall interaction patterns (Chee *et al* 2016), whereas the same group later proposed a simplified cylindrical phantom with a rigid inclusion (Chee *et al* 2018).

Although of interest, those phantoms are still incomplete and do not correspond to the geometry of vulnerable carotid atherosclerotic plaques containing a large lipid pool embedded within the vessel wall of an anthropomorphic lumen geometry. To our knowledge, no 3D phantom without any axis of symmetry (usually required when molding processes are used) and describing the geometry of common, internal and external carotid arteries, with a plaque in the carotid bulb characterized by a different mechanical property than the surrounding vessel wall, has been developed. Such phantoms are of interest to validate emerging imaging methods or for testing image artifacts, as exemplified in a recent elastography study where the phantom with a 70% stenosis proposed in the current study was used (Li *et al* 2018).

In this study, we designed a carotid bifurcation phantom with a soft inclusion covered by a mimicking atheroma cap. This article is describing the design and manufacturing process of the anthropomorphic phantom. In section 2, the different manufacturing steps are explained. Then, ultrasound images acquired to demonstrate the various features of the design are presented followed by the assessment of mechanical properties of the phantom using rheometer testing. Finally, a discussion exposes possibilities and limitations of the phantom.

2. Anthropomorphic phantom design

To fabricate a carotid bifurcation phantom for rheology studies, a digital geometry was used for the lumen stem design. This geometry was based on a computed tomography scan of a healthy individual that was used to create a finite elements model (Swillens *et al* 2009, Ekroll *et al* 2013). The phantom did not have any axis of symmetry and it corresponded to a realistic clinical case. In addition to the normal vessel geometry, a 70% stenosis model was considered. To produce the stenosed phantom, the vessel wall boundary was modified to include a plaque with an embedded inclusion, mimicking a soft lipid pool. Because the plaque included a single soft inclusion, its shape was determined by the geometry of the stenosis.

2.1. Digital plaque and inclusion design

The 3D geometry of the vessel lumen was downloaded (<http://www.biommeda.ugent.be/biomedical-ultrasound-research>, October 2016) and imported into a computer-aided design software (Solidworks, Dassault Systems, Waltham, MA). From this file, a normal carotid and a 70% stenosis lumen were produced. These two digital lumen geometries were considered for the design of different outer molds (figures 1(C) and (D)). The original geometry was digitally modified to extend the length of internal and external carotid arteries to center the bifurcation into the mold.

The lumen stem of the normal carotid phantom was used as reference geometry. To produce the stenosis, the lumen dimension at the bifurcation was reduced by adding a synthetic plaque producing a 70% stenosis. The plaque dimension was chosen to obtain an idealized anthropomorphic shape. The radial and longitudinal dimensions of the spline describing the seed shaped inclusion were 4.3 mm and 13.2 mm, respectively. From these dimensions, a spline (figure 1(A), spline 1) was drawn at the bulb on the outer wall of the internal carotid artery where the plaque naturally forms. The plaque thus corresponds to the volumetric intersection between the revolution of this spline around the axis (figure 1(A), line 2) and the healthy carotid lumen model. To create the soft inclusion, the same procedure was followed to produce a 1 mm equidistant spline toward the wall to create the atheroma cap (figure 1(A), spline 3). The resulting plaque looked like a lemon seed. The radial, axial and longitudinal dimensions of the soft inclusion were 3.8 mm, 9.1 mm and 5.7 mm, respectively. A cross section of the phantom mold at the

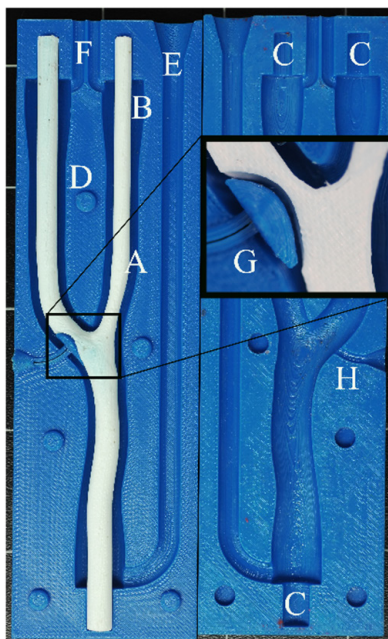


Figure 2. The 3 parts of the mold including the lumen stem in white and the 2 halves of the outer mold in blue. A 2 mm gap is let between the lumen stem and the outer mold to obtain a uniform wall thickness (label A). A thicker hollowness is seen at the extremities to create the sleeves (label B). The cylindrical extensions for the alignment of the lumen stems (label C) are carved into the outer mold. Casting ducts allow filling the mold to create the wall (labels E and F) or the lipid pool (label H). Five doll pins (label D) are included to ensure the alignment of the two halves. The zoomed insert shows the small ABS piece attached to one half of the outer mold (label G). This lemon seed shaped piece is used to create the pouch between the phantom wall and the atheroma cap for the fabrication of the mimicking lipid pool.

maximum stenosis is shown in figure 1(B). With this rendering, one could see the wall and atheroma cap in white (1), the soft inclusion in green (2), and the phantom with a stenosed lumen in red (3). Diameters of the geometry at the common (CCA), internal (ICA) and external (ECA) carotid arteries were 6.0 mm, 5.0 mm and 3.8 mm, respectively. The diameter of the non-obstructed bulb was 5.4 mm and it was reduced to 1.6 mm for producing the 70% stenosis (figures 1(C) and (D)). The length of each phantom was 123 mm.

2.2. Molding design

Molds made of acrylonitrile butadiene styrene (ABS) were 3D printed (Dimension Elite, Stratasys Inc., Eden Prairie, MN, USA) to create polyvinyl alcohol cryogel (PVA-C) phantoms. The outer molds consisted of two halves and a small piece that had to be removed to produce a pouch for the soft inclusion (figure 2, label G). The lumen stem inner mold allowed producing the lumen of the phantom (white Y geometry, figure 2). This geometry was chosen according to the degree of stenosis needed.

Here are the steps to make the lumen stem and then both halves of the outer mold. A cylindrical extension was added to each extremity of the digital vessel lumen geometry to allow radial alignment and longitudinal placement of the lumen stem into the outer mold (figure 2, label C). The thickness of the vessel wall was uniformly fixed at 2 mm by scaling the lumen stem to create an expanded geometry (figure 2, label A). To seal the extremities of the phantom onto external tubing for *in vitro* testing, the thickness of the sleeve was gradually increased to 3 mm (figure 2, label B).

Then, using the expanded geometry with sleeves, the Solidwork mold function allowed the creation of both halves by cutting the outer mold along the plane described by the center of the ECA and CCA at extremities, and the center of the soft inclusion in the sagittal plane. Five doll pins and corresponding holes were added to the halves for alignment purpose (figure 2, label D). Casting ducts were included to allow injection of PVA. For this purpose, ABS mold halves were closed and positioned vertically with both ICA and ECA ends on top. A first duct was made to allow PVA to enter the mold from the bottom to avoid formation of bubbles (figure 2, label E). Two more casting ducts were placed on top to allow exit of ambient air (figure 2, label F).

As introduced earlier, a small lemon seed shaped ABS piece was positioned in the carotid bulb to create the soft inclusion (figure 2, label G). The ABS piece was used to form a pouch into the phantom wall that allowed the second casting of the PVA to form the soft inclusion. This small piece was held in place by a casting duct attached to the outer mold. By the same way, the casting duct created a hole through the external wall of the pouch into which it became possible to remove the small piece of ABS before injecting the PVA. Since PVA-C is deformable, the casting duct did not need to be as large as the inclusion. A distance of 1 mm was maintained between the ABS piece and

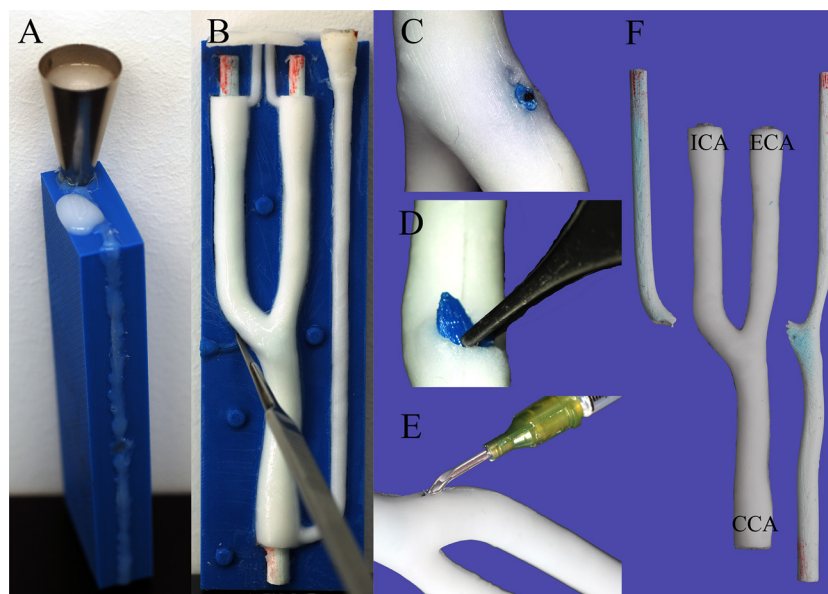


Figure 3. Phantom manufacturing steps: (A) The lumen stem is inserted into the outer halves and the mold is sealed with hot glue prior to injecting PVA into the main casting duct. (B) After five freeze-thaw cycles, the mold is opened and the casting duct connecting the small ABS piece to the outer mold halve is cut with a scalpel. The PVA-C remaining into the casting duct is also removed. (C) A zoom on the small piece of ABS trapped into the PVA-C phantom wall. (D) A zoom on the tweezer used to remove the small ABS piece through the hole left by the casting duct. (E) Injection of PVA inside the pouch with a syringe. (F) After a last freeze-thaw cycle, the lumen stem is broken and gently removed from the PVA-C atherosclerotic carotid bifurcation phantom. CCA: common carotid artery; ICA: internal carotid artery; ECA: external carotid artery.

the lumen stem to create the mimicked atheroma cap between the soft inclusion and the vessel lumen. With this fabrication process, the mechanical property of the atheroma cap was the same as that of the remaining vessel wall.

2.3. Manufacturing steps

Digital geometries of the molds and lumen stems were exported in stereo lithography file format and 3D printed. The mold halves and lumen stem were then covered with varnish (colorMaster, Krylon, Cleveland, OH, USA) to counteract the permeability of layered 3D printed ABS pieces. The mold design foresees two separate PVA injections, the first injection for manufacturing the phantom wall, and then the second injection to manufacture the soft inclusion. Here are the key steps of phantom production as depicted in figure 3. The lumen stem was inserted into the outer mold then the two halves were closed and sealed with thermoplastic glue; a funnel in which to pour the PVA later forming the phantom wall was added (figure 3(A)). A first injection of PVA allowed manufacturing the wall of the phantom and atheroma cap in one piece. Once the wall was stiffened after five freeze-thaw cycles, the two mold halves were opened (figure 3(B)). To produce the soft inclusion, the small ABS piece was gently cut with a scalpel from the outer mold halve and the carotid wall phantom was released from the outer mold. The PVA-C remaining within the casting duct was removed with scissor. The small ABS piece trapped into the phantom wall (figure 3(C)) was gently removed through the hole left by the casting duct with tweezers (figure 3(D)), by taking great care of not puncturing the mimicking atheroma cap. A second PVA injection was used to create the mimicking lipid pool with a different mechanical property. The empty cavity of the phantom was filled with PVA by taking care of not trapping air (figure 3(E)). The whole phantom experienced a last freeze-thaw cycle to fuse the soft inclusion with the vessel wall and mimicked atheroma cap. The Y shaped lumen stem remained trapped into the phantom. It was thus broken in two parts at the bifurcation prior to be extracted (figure 3(F)).

To facilitate the fracture, a donut-shaped weakness was previously created at the bifurcation on the ICA branch (figure 4(A)). The weakened section was filled with plasticine before the lumen stem was introduced into the outer mold (figure 4(B)). Care was taken to avoid geometry artifact by smoothing the plasticine to the neighboring stem section. It was not necessary to add a weakness for the 70% stenosis grade phantom since the stem was already fragile. Breaking the stem at the weakness (figure 4(C)) or at the site of the severe stenosis (figure 4(D)) allowed extracting the two parts by carefully pulling on them. The final phantom was then ready to use (figures 3(F) and 5).

2.4. PVA phantom material

The PVA solution used to manufacture the phantom consisted in 10% by weight of polyvinyl alcohol (batch # 407101, Vassal Brother Hospital, Beacon, NY, USA) mixed with pure water (Fromageau *et al* 2007). The solution was heated on a magnetic stirring plate until it was completely dissolved. To compensate for evaporation during

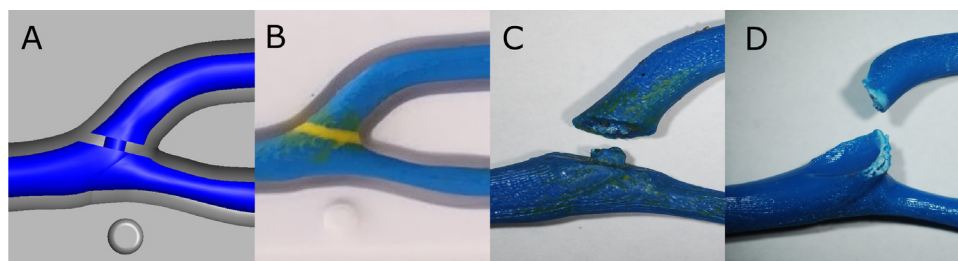


Figure 4. (A) A healthy geometry lumen stem showing the donut-shaped weakening. (B) A picture of the lumen stem with yellow plasticine. PVA-C was not poured yet into the mold for this example. (C) The lumen stem once broken can be extracted by carefully pulling on the two parts. (D) The 70% stenosis stem does not need extra weakening since the design is already fragile at the bifurcation.

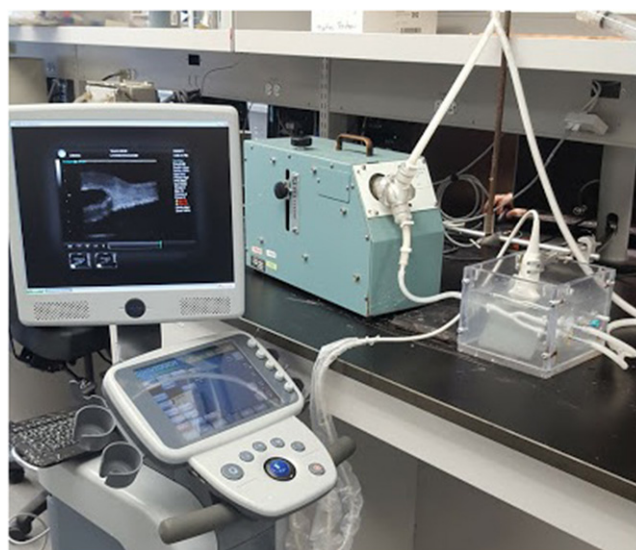


Figure 5. *In vitro* set-up for data acquisition. A Harvard pump was used to induce flow pulsatility into the phantom and vessel wall deformation. The Ultrasonix platform was used to acquire RF dataset for strain elastography evaluation.

dissolution, pure water was added to regain the initial weight. The solution was then mixed with 3% by weight of cellulose particles (Sigmacell, #S5504, Sigma Chemical, St. Louis, MO) to provide acoustic scatterers to the mixture. The PVA solution was injected into the mold at a temperature of 45 °C to facilitate filling through the casting ducts.

The polymerization of PVA occurred during 24 h of freezing-thawing cycles in a temperature-controlled chamber. The temperature cycle consisted in four steps. First, it varied from 20 to −20 °C over a period of 220 min at a controlled slope of −0.18 °C per minute. This was followed by a plateau of 500 min at −20 °C to stabilize the polymerization process. Then, a second ramp at a slope of +0.18 °C per minute brought back the temperature to 20 °C in 220 min. The last step of the cycle was a plateau of 500 min at 20 °C. As mentioned earlier, the wall and mimicked atheroma cap underwent six freeze-thaw cycles, whereas the soft inclusion experienced a single cycle.

2.5. Experimental setup

As illustrated in figure 5, the phantom was immersed in a container filled with a salted degassed water solution at 5% by weight ratio. We used salted water to reduce specular reflections around the phantom by matching ultrasound refractive indices (Porée *et al* 2015). Indeed, the acoustic impedance of saline is $1.62 \times 10^3 \text{ Kg m}^{-2} \text{ s}^{-1}$ (Kobayashi *et al* 2014) and that of PVA-C is $1.74 \times 10^3 \text{ Kg m}^{-2} \text{ s}^{-1}$ (Zell *et al* 2007), which is closer than the acoustic impedance of unsalted water ($1.50 \times 10^3 \text{ Kg m}^{-2} \text{ s}^{-1}$). A water mixture of cornstarch particles (1% weight ratio) mimicking scattering blood and dissolved salt (5% weight ratio) was pumped into the phantom with a pulsatile pump (model 1421, Harvard Apparatus, Holliston, MA, USA). The mean flow rate in the ICA was set to 360 ml min^{-1} using an electromagnetic flowmeter (Cliniflow II, Carolina Medical, East Bend, NC, USA) to match physiological conditions (Marshall *et al* 2004). A water column maintained a physiological pressure while allowing pressure variations induced by the pump. Systolic and diastolic pressures were set at 110 mmHg and 65 mmHg, and monitored with the ViVitest software system (Vivitro Labs Inc., Victoria, BC, Canada).

2.6. Experimental ultrasound acquisitions

To show the performance of vascular phantoms, both healthy and 70% stenosis phantoms were imaged in B-mode, color-Doppler and power-Doppler. For shear wave elastography and strain elastography, only the 70% stenosis phantom was scanned to depict mechanical properties of the mimicking atherosclerotic plaque.

2.6.1. B-mode images and thickness measurements

Dimensional measurements of the phantom were done on B-mode images, at atmospheric pressure, prior to starting pumping the mimicking blood. The phantom was scanned with an Aixplorer ultrasound system (Supersonic Imagine, Aix-en-Provence, France) using the SL15-4 probe. The distance measurement tool was used for ICA, ECA and CCA inner diameters, wall thickness and stenosis grade. Five measurements of the inner lumen diameters were done in longitudinal view for both phantoms. The wall thickness was assessed in cross-sectional view by performing eight radial measurements to assess the concentricity of the lumen and vessel wall. The stenosis grade was measured on cross-sectional images using the european carotid surgery trial (ECST) method by determining the outer vessel diameter and lumen diameter at the maximum stenosis position (Warlow 1998).

2.6.2. Color and power Doppler

Ultrasound Doppler images of the immersed phantom with circulating mimicking blood were recorded by the Aixplorer system. Images were acquired in longitudinal view under similar flow condition (see section 2.5 experimental setup). The Doppler maximum velocity was set to $\pm 51 \text{ cm s}^{-1}$ and the field of view included the ICA, ECA and CCA.

2.6.3. Shear wave elastography

The Aixplorer system was also used in shear wave elastography (SWE) mode to evaluate the phantom elasticity. The phantom was not pressurized during SWE acquisitions. The proprietary measuring tool 'Q-Box' allowed to quantitatively measure the mean elasticity over a region of interest (ROI). For both phantom regions (wall and soft inclusion), the mean shear elasticity moduli was averaged from 5 Q-Boxes positioned on different images. Mechanical properties of the phantom were also assessed using mechanical testing (see section 2.7).

2.6.4. Strain elastography

Measurements of the axial strain and axial shear strain were carried out on a series of ultrasonic radio frequency (RF) images of the phantom. A sequence including three pumping cycles, at a frame rate of 47 images s^{-1} , was recorded with a SonixTouch system (BK Medical, Peabody, Ma, USA) in research mode using an L14-5/38 linear array probe. The probe was fixed in longitudinal view over the bifurcation of the phantom (figure 5). RF images were post-processed as described in Roy-Cardinal *et al* (2017) and Cloutier *et al* (2018). Briefly, the software uses an optical flow-based Lagrangian speckle model estimator (LSME) to compute the deformation inside small ROIs over a segmented part of successive RF images. The axial strain and axial shear strain were computed distinctively over the wall and soft inclusion. The axial strain corresponds to compression (negative values) or dilation (positive values) of the tissue along the ultrasound beam. The axial shear strain measures an angular deformation and it was expressed in absolute value (i.e. magnitude).

2.7. Mechanical testing of phantom components

The mechanical properties of the PVA-C phantom were measured using a Bose Electroforce 3220 rheometer (TA instrument, New Castle, DE, USA). The method used for these tests was described earlier (Fromageau *et al* 2007). Briefly, a uniaxial tensile test was performed while the sample undergone a maximum elastic deformation of 30% or 66% for the wall and mimicking soft inclusion, respectively. Elasticity tests of the wall material were made on cylindrical sections of 3.6 mm in diameter of the PVA-C extracted from the mold casting duct. For mechanical testing of the PVA-C inclusion, a 4.4 mm diameter cylindrical sample was created by aspiration of the liquid PVA through the bore of a 1 ml syringe. The solidified sample was removed from the syringe for mechanical tests. Young's moduli were calculated as the mean slope of the stress-strain curve in the linear part. Reported elasticity moduli correspond to the mean of eight measurements \pm standard deviation.

2.8. Verification of the geometry of the soft inclusion

The PVA material used for the vessel wall and soft inclusion had similar acoustic properties. It was therefore anticipated that the contrast between both parts of the phantom would not be good enough to differentiate them on B-mode images. To demonstrate that the geometry of the inclusion corresponded to that expected during molding, a modified phantom with a PVA-C inclusion containing a high concentration of carbon fibers (visually black) rather than cellulose particles (visually white) was fabricated. This way it was possible to visually see the inclusion with contrasted optical images. Details on the fabrication process are provided in Appendix.

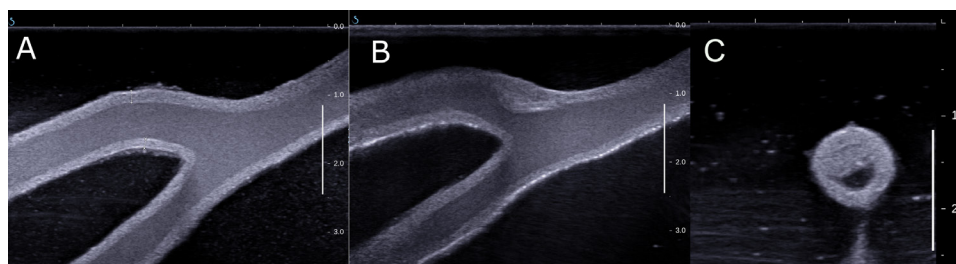


Figure 6. B-mode images of (A) the healthy phantom and (B) the 70% stenotic phantom in longitudinal view. (C) A cross sectional view of the carotid artery phantom showing the 70% stenosis located at the bulb. The image plane was selected to optimize the visibility of the stenosis, as the anthropomorphic phantom corresponds to a realistic clinical case with no 3D axis of symmetry.

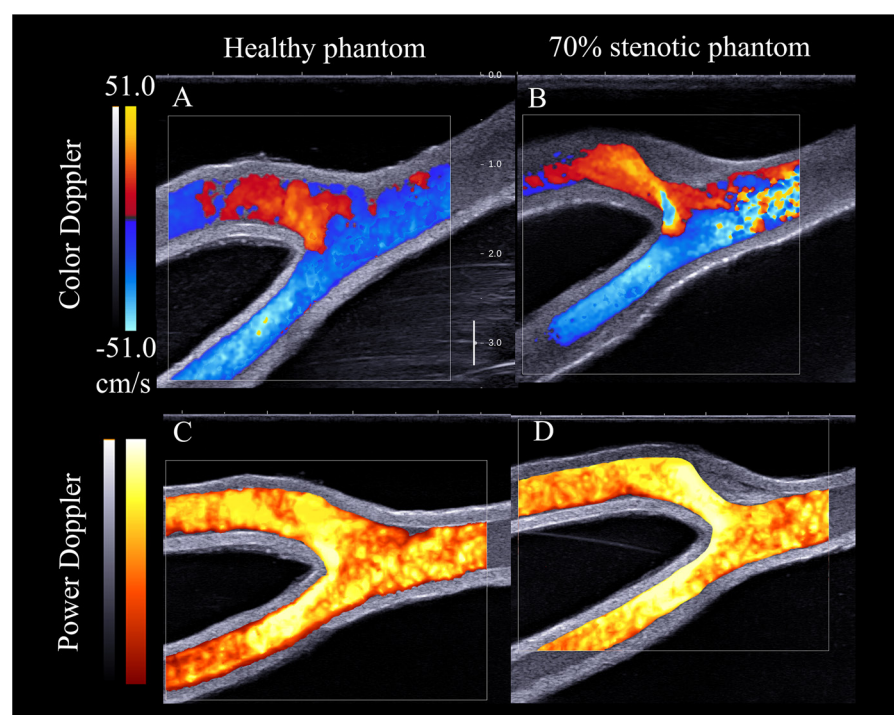


Figure 7. Color Doppler ((A) and (B)) and power Doppler ((C) and (D)) images of the carotid bifurcation artery phantom. (Right) The healthy vessel. (Left) The 70% stenotic internal carotid artery. Images were acquired at the systolic peak pressure (110 mmHg) under *in vitro* conditions.

3. Results

3.1. Ultrasound imaging of the phantoms

3.1.1. B-mode images and thickness measurements

A homogeneous wall thickness was obtained for the 0% stenosis phantom all along the mimicking artery (figure 6(A)). On B-mode images of the 70% stenosis phantom, the soft inclusion was not easily distinguishable from the vessel wall and atheroma cap because echogenicity was similar (figure 6(B)). The stenosis grade was determined based on the non-pressurized phantom dimensions. The measured stenosis grade was 67% instead of the expected 70% stenosis (figure 6(C)). The mean thickness of the healthy phantom wall section was 1.7 ± 0.2 mm (coefficient of variation of 12%). For the 70% stenosis phantom, lumen diameters of 5.6 ± 0.1 mm, 4.9 ± 0.1 mm and 3.7 ± 0.1 mm were measured for the CCA, ICA and ECA, respectively.

3.1.2. Color and power Doppler

The ability of the phantom to describe physiological flow was evaluated in color and power Doppler modes at the same flow and pressure conditions for both unobstructed and 70% stenosis phantoms. On color Doppler images, flow velocity acceleration was seen in the ECA and a jet appeared in the ICA for the severe stenosis case (figure 7 top right). Power Doppler images showed quite uniform backscatter

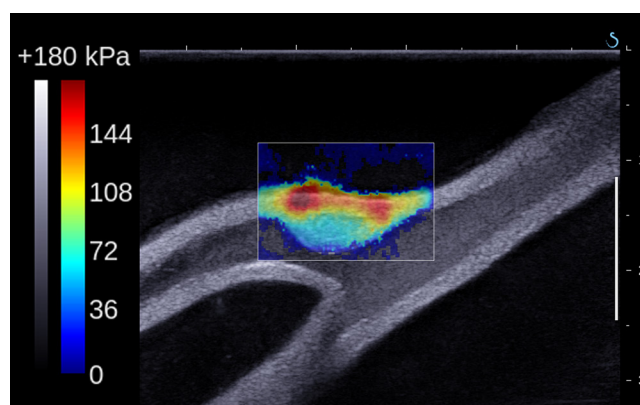


Figure 8. Shear wave elasticity images of the 70% stenosis phantom showing different elasticity moduli for the plaque and vessel wall.

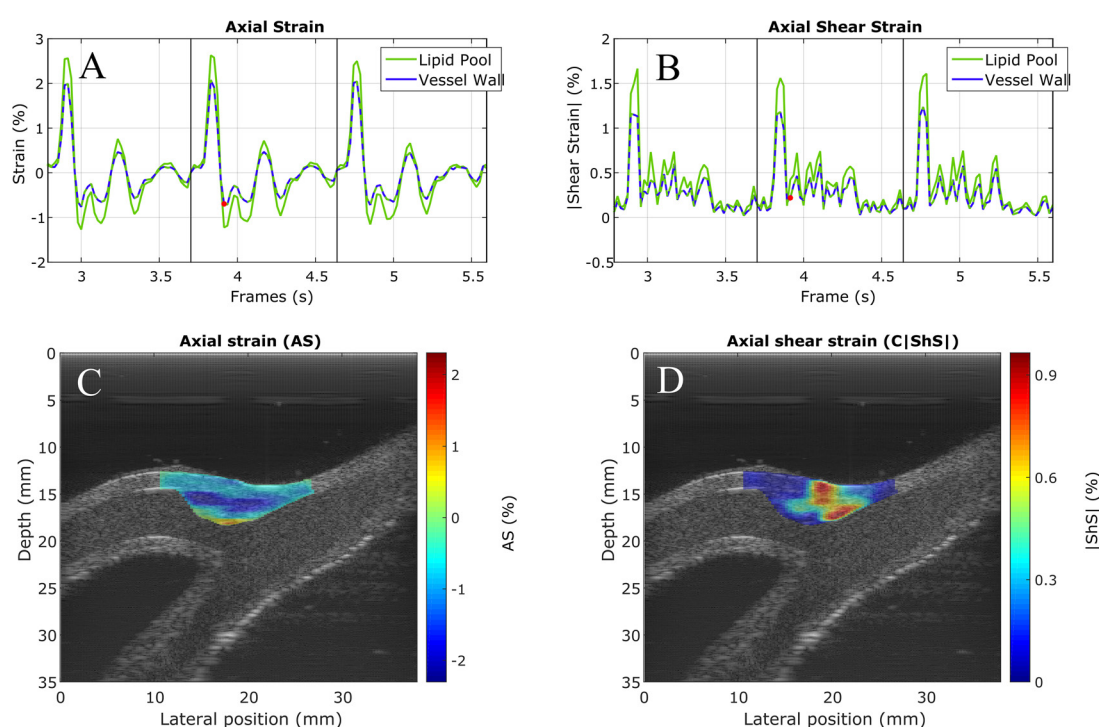


Figure 9. Strain elastography results for the 70% stenosis phantom. (A) and (B) The time-varying mean axial strain and axial shear strain magnitude for the mimicking lipid pool (green line) and wall (blue line). (C) and (D) The instant axial strain map and instant axial shear strain magnitude map for time corresponding to the green dot in (A) and (B).

power over the ICA, ECA and CCA. The stenotic lumen was well identified in both Doppler modes (figure 7 right).

3.1.3. Shear wave elastography

Figure 8 shows an example of a shear wave elastography image of the 70% stenosis phantom. Statistics over five images revealed a mean shear elasticity modulus of 127 ± 10 kPa for the phantom wall. The elasticity of the mimicking lipid pool was lower (i.e. softer) with an averaged value of 66 ± 13 kPa.

3.1.4. Strain elastography

Strain elastography was performed over ROIs delimited by the stenotic zone (figure 9). Figure 9(A) and (B) shows the axial strain and axial shear strain magnitude over time for three pumping cycles. The wall and mimicking lipid pool deformation curves are shown separately (blue and green lines, respectively). The wall and plaque deformations over time were synchronized, with maximum magnitude of the axial strain and axial shear strain occurring within the soft inclusion. For both ROIs, the maximum deformation peak was higher

for the axial strain (2.6%) than for the axial shear strain (1.7%). Figure 9(C) and (D) shows instant axial strain and axial shear strain magnitude superimposed on B-mode images. More axial deformation is seen within the mimicking lipid pool than surrounding wall components. A shear strain concentration with high magnitudes is observed within the soft inclusion (figure 9(D)).

3.2. Mechanical testing of phantom components

Young's moduli obtained during mechanical tests provided values of 342 ± 25 kPa for the wall and 17 ± 3 kPa for the soft inclusion.

3.3. Geometry of the soft inclusion

As noticed in figure 6(B) and (C), the geometry of the inclusion was hardly visible on B-mode images. The visual assessment of the inclusion is given in appendix.

4. Discussion

4.1. Realism of the anthropomorphic carotid artery phantoms

According to Steinman *et al* (2002), the wall thickness of 59 years old men with asymptomatic carotid artery disease varies from 0.5 to 2.5 mm with an approximated mean vessel wall of 1.2 mm. The thickness of the wall of phantoms manufactured with the proposed fabrication process was 1.7 ± 0.2 mm (figure 6). Notice that the thickness obtained is smaller than the mold wall interspace of 2.0 mm (figure 2). The reduction in dimension of PVA-C during polymerization with several freeze-thaw cycles (six in our case) was also observed by Chu and Rutt (1997). Nevertheless, B-mode images (figure 6) showed constant dimension for the whole mimicking artery (coefficient of variation of 12%). A main advantage of the proposed fabrication process is that the geometry of the inclusion is no longer limited to a rectilinear vessel structure, as in Chu and Rutt (1997), Maurice *et al* (2005), Le Floc'h *et al* (2010), Abran *et al* (2014), Majdouline *et al* (2014) and Porée *et al* (2015, 2017), or a structure made of concentric layers (Brusseau *et al* 2001, Chee *et al* 2018). It is also compliant with realistic elasticity moduli, which is a major advantage as it provides the opportunity of studying fluid-wall interaction phenomena, which is not possible with rigid or semi-rigid anthropomorphic carotid artery phantoms (Moore *et al* 1999, Ionita *et al* 2014).

The elasticity values of our phantom at 342 ± 25 kPa for the wall and 17 ± 3 kPa for the soft inclusion are consistent with Fromageau *et al* (2007) when considering the same number of PVA-C freeze-thaw cycles. According to Riley *et al* (1992), the Young's modulus of atherosclerotic carotid arteries ranges from 701 ± 324 kPa to 983 ± 557 kPa, as a function of pressure range, sex, and age, which let a quite large range of elasticity for pathological walls. Local compressive tests revealed a wider range of Young's moduli from 6 to 891 kPa for human carotid plaques (Chai *et al* 2013). According to Keeny and Richardson (1987), the Young's modulus of lipid pools is 100 times smaller than a normal artery wall, which has been measured non-invasively at 630 ± 210 kPa by Selzer *et al* (2001). The elasticity of the soft inclusion was 17 ± 3 kPa in our study. It was therefore close to the estimated value of 6 ± 2 kPa assessed by Keeny and Richardson (1987). However, the Young's modulus of the PVA-C mimicking the vessel wall was under maximum values reported in the literature. Using more freeze-thaw cycles would provide the possibility of rigidifying the wall (Young's moduli of 615 ± 70 kPa were obtained by Fromageau *et al* (2007) using ten freeze-thaw cycles). With the possibility to adjust the Young's modulus of the wall independently of that of the inclusion by varying the PVA concentration or the number of freeze-thaw cycles, this phantom is well suited for many applications. In figure 9, the instantaneous axial shear strain reveals a construction artifact in the upper wall created by the casting duct that was filled afterward with the inclusion material. To avoid this limitation, the casting could be moved on the side of the phantom so the artifact would be away of the longitudinal or cross sectional view used for clinical diagnosis.

4.2. Advantages for ultrasound imaging developments

Over the last decade, the realism of vascular phantoms continued to be improved. If PVA-C remains widely used for vascular phantoms, the shape has changed from homogeneous wall phantoms (Ribbers *et al* 2007, Li *et al* 2017) to phantoms embedding one rectilinear inclusion (Korukonda and Doyley 2012, Porée *et al* 2015). Then, phantoms with multiple rectilinear inclusions made of materials with different elasticity were proposed (Porée *et al* 2017). As it was the case for the phantom of Chee *et al.* (2016), the present study described a fabrication process to produce physiologically shaped carotid artery phantoms for ultrasound applications.

In this paper, we have presented examples of clinical ultrasound images (B-mode, color Doppler, power Doppler and shear wave elastography), imaging modalities not yet implemented on clinical systems (axial strain and axial shear strain elastography), and an optical image used for validation (see appendix). These images could

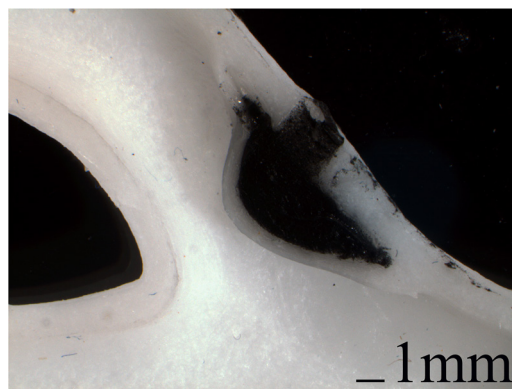


Figure 10. Microscopy optical image of the phantom showing the constituents of the plaque. The lipid inclusion was intentionally colored in black to show the atheroma cap surrounding it. Dark artifacts are noticed on the atheroma cap and this corresponds to residual carbon fibers that leaked between both parts of the mold.

validate the phantom geometry and mechanical characteristics (flow and elasticity). As mentioned by Chai *et al* (2013), elasticity measurements presented in the literature have high variability and several state-of-the-art measurement methods were used. As reviewed by them, atomic force microscopy indentation is now elucidating smaller stiffness than expected for atherosclerotic vessel structures. That point to the necessity of improving *in vivo* elasticity measurement methods to characterize arteries.

In 2010, Couade *et al* showed the feasibility of arterial wall shear wave elasticity imaging with a simple agar phantom and *in vivo* on a healthy carotid artery. Later, Ramnarine *et al* (2014) studied the reproducibility of SWE with a simplistic, rectilinear stenosis phantom showing heterogeneous mechanical properties. Despite the fact that no mechanical testing of the mimicking material (butter and PVA-C) were made, SWE images provided quantitative elasticity measurements of 43 kPa and 170 kPa for soft and hard inclusions, respectively. Other groups have designed PVA-C artery phantoms to validate the angle-independence of principal strain elastography measurements (Nayak *et al* 2018). Their homogenous phantom wall elasticity was mechanically measured at 42 kPa. Maksuti *et al* (2016) reported different elasticity accuracy regarding the shear wave elastography method used to characterize their PVA-C carotid artery phantom. They found better results using the shear wave phase velocity. The same group also tested two phantoms each containing a simplified inclusion more rigid or softer than the wall of the phantom (Widman *et al* 2015). They showed that their post-processing (phase velocity) allowed to dynamically measure elasticity values. A limitation of this study concerns dimensions of plaques and walls that were unrealistic. Dumont *et al* (2009) compared shear wave velocity ratios of inner and outer walls of their phantom. They found that acoustic radiation force impulse (ARFI) velocity ratios were not consistent with mechanical testing but the ultrasound method was sufficiently accurate to qualitatively differentiate the two components of the phantom.

In our study, SWE measurements showed mean shear wave elasticity moduli of 127 kPa for the wall and 66 kPa for the soft inclusion. Mechanical testing gave mean Young's moduli of 342 kPa for the wall and 17 kPa for the inclusion. Assuming a Poisson ratio of 0.5 for PVA-C, as measured by Fromageau *et al* (2007) (i.e. incompressible for which $3 \times \text{shear modulus} = \text{Young's modulus}$), mechanical testing thus corresponds to shear moduli of 114 kPa for the wall and 6 kPa for the inclusion. Good agreement was thus obtained for PVA-C experiencing six freeze-thaw cycles (wall). However, the explanation of the difference between mechanical rheology and supersonic shear imaging measurements in the case of the soft inclusion would require additional validation. Anchoring slippery conditions during tensile tests with the soft PVA-C experiencing a single freeze-thaw cycle may be the explanation.

5. Conclusion

Each new ultrasound imaging modality brings a lot of challenges during *in vitro* validation. Our new phantoms are not only compatible with ultrasound imaging, but also reflect the shape and mechanical characteristics of normal and pathological stenosed carotid arteries. Phantoms are no more limited to morphological imaging nor flow, but can also contribute to the development of vascular and tissue rheology methods. With the fabrication method described in this article, we showed how to design a carotid bifurcation phantom that has a wall stiffer than the inclusion. Moreover, this phantom can withstand physiological pressures and reproduce conditions of carotid atherosclerotic plaque evolution (different stenosis grades can be fabricated using the same fabrication process). We believe that this innovative method can be applied to manufacture phantoms mimicking other pathologies such as abdominal aortic aneurysms or venous thrombosis.

Acknowledgments

This work was supported by the Collaborative Health Research Program of the Natural Sciences and Engineering Research Council of Canada (CHRP-462240-2014) and the Canadian Institutes of Health Research (CPG-134748).

Appendix

This section is presenting a validation method to demonstrate that the geometry of the mimicking plaque matched that expected by the manufacturing process. A specific phantom was produced for this purpose. To visually differentiate the soft inclusion from the phantom wall and atheroma cap, the mix of PVA and cellulose particles was replaced by a solution of PVA containing carbon fibers. The same mold and manufacturing method were used to produce this phantom. The solution consisted in 10% by weight of PVA, 3% by weight of 20 microns carbon powder (Sigma-Aldrich, #282863), and 87% of deionised water. The inclusion was jellified using one freeze-thaw cycle and the remaining phantom components experienced six freeze-thaw cycles. To visualise the plaque, the phantom was cut longitudinally and imaged with a microscope. The dimension of the soft inclusion and plaque constituents were measured with the freeware MicroDicom (Sofia, Bulgaria). Ten thickness measurements were taken along the atheroma cap; mean \pm one standard deviation are reported.

Figure 10 shows the different parts of the plaque. The black soft inclusion was well delimited and visible on the image. The atheroma cap and vessel wall appear in white. The axial and longitudinal dimensions of the inclusion on this slice are 2.7 mm and 6.9 mm, respectively. The thickness of the atheroma cap was measured at 0.6 ± 0.07 mm. The axial and longitudinal dimensions of the plaque on this image are 3.5 mm by 11.3 mm, respectively.

Although of interest to visualize the constituents of the plaque, the image in figure 10 corresponds to a 2D projection of the 3D plaque geometry. The plane selected for this example does not correspond perfectly to the plane of the maximum occlusion. Therefore, reported plaque dimensions do not correspond exactly to the computed-aided design drawing. However, this validation allowed appreciating the geometry of the inclusion and presence of the mimicking atheroma cap.

ORCID iDs

Richard Lopata  <https://orcid.org/0000-0001-6618-6184>

Guy Cloutier  <https://orcid.org/0000-0002-4957-4844>

References

- Abram M, Cloutier G, Roy Cardinal M H, Chayer B, Tardif J C and Lesage F 2014 Development of a photoacoustic, ultrasound and fluorescence imaging catheter for the study of atherosclerotic plaque *IEEE Trans. Biomed. Circuits Syst.* **8** 696–703
- Brusseau E, Fromageau J, Finet G, Delachartre P and Vray D 2001 Axial strain imaging of intravascular data: results on polyvinyl alcohol cryogel phantoms and carotid artery *Ultrasound Med. Biol.* **27** 1631–42
- Chai C K, Akyildiz A C, Speelman L, Gijzen F J, Oomens C W, van Sambeek M R, van der Lugt A and Baaijens F P 2013 Local axial compressive mechanical properties of human carotid atherosclerotic plaques—characterisation by indentation test and inverse finite element analysis *J. Biomech.* **46** 1759–66
- Chee A J, Ho C K, Yiu B Y and Yu A C H 2016 Walled carotid bifurcation phantoms for imaging investigations of vessel wall motion and blood flow dynamics *IEEE Trans. Ultrason. Ferroelectr. Freq. Control* **63** 1852–64
- Chee A J, Yiu B Y, Ho C K and Yu A C H 2018 Arterial phantoms with regional variations in wall stiffness and thickness *Ultrasound Med. Biol.* **44** 872–83
- Chu K C and Rutt B K 1997 Polyvinyl alcohol cryogel: an ideal phantom material for MR studies of arterial flow and elasticity *Magn. Reson. Med.* **37** 314–9
- Cloutier G, Roy Cardinal M H, Ju Y, Giroux M F, Lanthier S and Soulez G 2018 Carotid plaque vulnerability assessment using ultrasound elastography and echogenicity analysis *Am. J. Roentgenol.* **211** 847–55
- Couade M, Pernot M, Prada C, Messas E, Emmerich J, Bruneval P, Criton A, Fink M and Tanter M 2010 Quantitative assessment of arterial wall biomechanical properties using shear wave imaging *Ultrasound Med. Biol.* **36** 1662–76
- Dumont D, Dahl J, Miller E, Allen J, Fahey B and Trahey G 2009 Lower-limb vascular imaging with acoustic radiation force elastography: demonstration of *in vivo* feasibility *IEEE Trans. Ultrason. Ferroelectr. Freq. Control* **56** 931–44
- Eklroll I K, Swillens A, Segers P, Dahl T, Torp H and Lovstakken L 2013 Simultaneous quantification of flow and tissue velocities based on multi-angle plane wave imaging *IEEE Trans. Ultrason. Ferroelectr. Freq. Control* **60** 727–38
- Fekkes S, Saris A E, Menssen J, Nillesen M M, Hansen H H and de Korte C L 2018 Multi-plane ultrafast compound 3D strain imaging: experimental validation in a carotid bifurcation phantom *Appl. Sci.* **8** 637
- Fromageau J, Gennisson J L, Schmitt C, Maurice R L, Mongrain R and Cloutier G 2007 Estimation of polyvinyl alcohol cryogel mechanical properties with four ultrasound elastography methods and comparison with gold standard testings *IEEE Trans. Ultrason. Ferroelectr. Freq. Control* **54** 498–509
- Ionita C N, Mokin M, Varble N, Bednarek D R, Xiang J, Snyder K V, Siddiqui A H, Levy E I, Meng H and Rudin S 2014 Challenges and limitations of patient-specific vascular phantom fabrication using 3D Polyjet printing *Proc. SPIE* **9038** 90380M
- Keeny S M and Richardson P D 1987 Stress analysis of atherosclerotic arteries *Eng. Med. Biol. Soc.* **46** 1484–5

- Kobayashi K, Yoshida S, Saijo Y and Hozumi N 2014 Acoustic impedance microscopy for biological tissue characterization *Ultrasonics* **54** 1922–8
- Korukonda S and Doyle M M 2012 Visualizing the radial and circumferential strain distribution within vessel phantoms using synthetic-aperture ultrasound elastography *IEEE Trans. Ultrason. Ferroelectr. Freq. Control* **59** 1639–53
- Lai S S, Yiu B Y, Poon A K and Yu A C H 2013 Design of anthropomorphic flow phantoms based on rapid prototyping of compliant vessel geometries *Ultrasound Med. Biol.* **39** 1654–64
- Le Floc'h S, Cloutier G, Finet G, Tracqui P, Pettigrew R I and Ohayon J 2010 On the potential of a new IVUS elasticity modulus imaging approach for detecting vulnerable atherosclerotic coronary plaques: *in vitro* vessel phantom study *Phys. Med. Biol.* **55** 5701–21
- Li G Y, He Q, Xu G, Jia L, Luo J and Cao Y 2017 An ultrasound elastography method to determine the local stiffness of arteries with guided circumferential waves *J. Biomech.* **51** 97–104
- Li H, Chayer B, Roy Cardinal M H, Muijsers J, van den Hoven M, Qin Z, Gesnik M, Soulez G, Lopata R and Cloutier G 2018 Investigation of out-of-plane motion artifacts in 2D noninvasive vascular ultrasound elastography *Phys. Med. Biol.* **63** 245003
- Majdouline Y, Ohayon J, Keshavarz-Motamed Z, Roy Cardinal M H, Garcia D, Allard L and Cloutier G 2014 Endovascular shear strain elastography for the detection and characterization of the severity of atherosclerotic plaques: *in vitro* validation and *in vivo* evaluation *Ultrasound Med. Biol.* **40** 890–903
- Maksuti E, Widman E, Larsson D, Urban M W, Larsson M and Bjällmark A 2016 Arterial stiffness estimation by shear wave elastography: validation in phantoms with mechanical testing *Ultrasound Med. Biol.* **42** 308–21
- Marshall I, Papanthanasopoulou P and Wartolowska K 2004 Carotid flow rates and flow division at the bifurcation in healthy volunteers *Physiol. Meas.* **25** 691–7
- Maurice R L, Daronat M, Ohayon J, Stoyanova E, Foster F S and Cloutier G 2005 Non-invasive high-frequency vascular ultrasound elastography *Phys. Med. Biol.* **50** 1611–28
- Meagher S, Poepping T L, Ramnarine K V, Black R A and Hoskins P R 2007 Anatomical flow phantoms of the nonplanar carotid bifurcation, Part II: experimental validation with Doppler ultrasound *Ultrasound Med. Biol.* **33** 303–10
- Mercure E, Destremes F, Roy Cardinal M H, Porée J, Soulez G, Ohayon J and Cloutier G 2014 A local angle compensation method based on kinematics constraints for non-invasive vascular axial strain computations on human carotid arteries *Comput. Med. Imaging Graph.* **38** 123–36
- Moore J A, Steinman D A, Holdsworth D W and Ethier C R 1999 Accuracy of computational hemodynamics in complex arterial geometries reconstructed from magnetic resonance imaging *Ann. Biomed. Eng.* **27** 32–41
- Nandall S D and Konofagou E E 2016 Assessing the stability of aortic aneurysms with pulse wave imaging *Radiology* **281** 772–81
- Nayak R, Schifitto G and Doyle M M 2018 Visualizing angle-independent principal strains in the longitudinal view of the carotid artery: phantom and *in vivo* evaluation *Ultrasound Med. Biol.* **44** 1379–91
- O'flynn P M, Roche E T and Pandit A S 2005 Generating an *ex vivo* vascular model *Asaio J.* **51** 426–33
- Pedersen M M, Pihl M J, Haugaard P, Hansen K L, Lange T, Lönn L, Nielsen M B and Jensen J A 2014 Novel flow quantification of the carotid bulb and the common carotid artery with vector flow ultrasound *Ultrasound Med. Biol.* **40** 2700–6
- Poepping T, Nikolov H N, Thorne M L and Holdsworth D W 2004 A thin-walled carotid vessel phantom for Doppler ultrasound flow studies *Ultrasound Med. Biol.* **30** 1067–78
- Porée J, Garcia D, Chayer B, Ohayon J and Cloutier G 2015 Noninvasive vascular elastography with plane strain incompressibility assumption using ultrafast coherent compound plane wave imaging *IEEE Trans. Med. Imaging* **34** 2618–31
- Porée J, Chayer B, Soulez G, Ohayon J and Cloutier G 2017 Noninvasive vascular modulography method for imaging the local elasticity of atherosclerotic plaques: Simulation and *in vitro* vessel phantom study *IEEE Trans. Ultrason. Ferroelectr. Freq. Control* **64** 1805–17
- Ramnarine K V, Garrard J W, Dexter K, Nduwayo S, Panerai R B and Robinson T G 2014 Shear wave elastography assessment of carotid plaque stiffness: *in vitro* reproducibility study *Ultrasound Med. Biol.* **40** 200–9
- Ribbers H, Lopata R G, Holewijn S, Pasterkamp G, Blankensteijn J D and de Korte C L 2007 Noninvasive two-dimensional strain imaging of arteries: Validation in phantoms and preliminary experience in carotid arteries *in vivo* *Ultrasound Med. Biol.* **33** 530–40
- Riley W A, Barnes R W, Evans G W and Burke G L 1992 Ultrasonic measurement of the elastic modulus of the common carotid artery. The Atherosclerosis Risk in Communities (ARIC) study *Stroke* **23** 952–6
- Roy-Cardinal M H, Heusinkveld M H G, Qin Z, Lopata R G P, Naim C, Soulez G and Cloutier G 2017 Carotid artery plaque vulnerability assessment using noninvasive ultrasound elastography: validation with MRI *Am. J. Roentgenol.* **209** 142–51
- Selzer R H, Mack W J, Lee P L, Kwong-Fu H and Hodis H N 2001 Improved common carotid elasticity and intima-media thickness measurements from computer analysis of sequential ultrasound frames *Atherosclerosis* **154** 185–93
- Shahmirzadi D, Li R X and Konofagou E E 2012 Pulse-wave propagation in straight-geometry vessels for stiffness estimation: theory, simulations, phantoms and *in vitro* findings *J. Biomech. Eng.* **134** 114502
- Steinman D A, Thomas J B, Ladak H M, Milner J S, Rutt B K and Spence J D 2002 Reconstruction of carotid bifurcation hemodynamics and wall thickness using computational fluid dynamics and MRI *Magn. Reson. Med.* **47** 149–59
- Swillens A, Lovstakken L, Kips J, Torp H and Segers P 2009 Ultrasound simulation of complex flow velocity fields based on computational fluid dynamics *IEEE Trans. Ultrason. Ferroelectr. Freq. Control* **56** 546–56
- Warlow C and European Surgery Trialists' Collaborative Groups 1998 Randomised trial of endarterectomy for recently symptomatic carotid stenosis: final results of the MRC European Carotid Surgery Trial (ECST) *Lancet* **351** 1379–87
- Widman E, Maksuti E, Larsson D, Urban M W, Bjällmark A and Larsson M 2015 Shear wave elastography plaque characterization with mechanical testing validation: a phantom study *Phys. Med. Biol.* **60** 3151–74
- Yiu B Y S, Lai S S M and Yu A C H 2014 Vector projectile imaging: time-resolved dynamic visualization of complex flow patterns *Ultrasound Med. Biol.* **40** 2295–309
- Zell K, Sperl J I, Vogel M W, Niessner R and Haisch C 2007 Acoustical properties of selected tissue phantom materials for ultrasound imaging *Phys. Med. Biol.* **52** N475–84